ADVANCED MATERIALS
www.advmat.de

Reprogrammable Dual-Regulated Pollen Actuators for Geometric Encoding

Jingyu Deng, Ze Zhao, Albar Ahmad, Jian Li, Young Hwan Choe, Yu Chien Lin, Shahrudin Ibrahim Mohammed, Chenchen Zhou, and Nam-Joon Cho**

Bilayer actuators capable of autonomously responding to complex environmental stimuli have attracted increasing interest for their potential in intelligent and multifunctional systems. Yet, achieving simultaneous programming and reprogramming of shape transformations in both active and passive layers through scalable, sustainable methods remains a significant challenge. Here, a novel bilayer actuator derived from naturally abundant pollen is reported, offering unprecedented dual-layer re-programmability. The passive layer, composed of digitally patterned toner, dictates the deformation direction, with the folding angles ranging from 0° to ≈152°. Meanwhile, the active pollen layer exhibits tunable humidity responsiveness modulated by pH, controlling actuation curvature ranging from 0.036 to 0.28 cm cm^{-1} and response speed ranging from 1.04 to 0.15° s^{-1}. Notably, the entire bilayer system can be fully disassembled via a mild, one-pot alkaline process, enabling more than 10 cycles of complete reprogramming without structural degradation. This dual-regulated architecture supports complex 3D geometric transformations and is demonstrated as a carrier of confidential information, encoding data through morphing analogs of encrypted binary code. By integrating programmable mechanics, renewable biomaterials, and energy-efficient reusability, this work establishes an eco-friendly and versatile platform for next-generation responsive materials and encrypted smart devices.

1. Introduction

Soft actuators, inspired by the adaptive deformation capabilities observed in natural organisms, have aroused tremendous attention due to their potential in next-generation soft robotics,[1,2] intelligent sensors,[3] and artificial muscles.[4,5] These actuators can convert diverse external stimuli, including heat,[6] light,[7,8] humidity,[9,10] electric, and magnetic fields,[11,12] into mechanical motions.[3,13] Soft actuators are typically composed of a bilayer structure consisting of an active, stimuli-responsive layer and a passive structure-supporting layer.[14] Upon external stimulation, the active layer undergoes deformation, creating differential strain against the passive layer, thus driving directional shape transformations. However, this bilayer architecture typically enables simple deformation modes, such as unidirectional bending or rolling,[15–17] limiting the complexity and versatility necessary for advanced applications. Sophisticated technologies, such as multifunctional devices or adaptive robotics, demand more programmable shape morphologies, like twisting or spiraling, that are challenging to achieve using conventional bilayer actuators.

Currently, the programming of complex deformation is primarily achieved through lithography,[18] laser direct writing,[19] and 3D/4D printing.[4,20] These methods, however, necessitate time-intensive template predesigning with limited scalability and require high cost.[4,20,21] Alternative strategies based on gradient structures, such as variations in crosslinker concentration,[22] fiber alignment,[9] molecular chain alignment,[17] or additive distributions,[23] allow complex 3D deformation but require meticulous molecular layer design,[13] external forces,[1,2] or precise additive adjustments.[11] Existing approaches control only one layer of the bilayer structure, significantly limiting actuation flexibility and programmability (**Figure 1A**). Most current humidity-responsive actuators also only allow programmability on a single layer, as illustrated in Table S1 (Supporting Information). Although some of them have exhibited limited re-programmability, their reconfigurations were typically constrained by the initial programming framework, lacking the

J. Deng, A. Ahmad, J. Li, Y. H. Choe, Y. C. Lin, S. I. Mohammed, C. Zhou, N.-J. Cho
School of Materials Science and Engineering
Centre for Cross Economy Global
Nanyang Technological University
50 Nanyang Drive, Singapore 637553, Singapore
E-mail: njcho@ntu.edu.sg

Z. Zhao
Hubei Key Laboratory of Biomass Resource Chemistry and Environmental Biotechnology
Hubei International Scientific and Technological Cooperation Base of Sustainable Resource and Energy
Hubei Engineering Center of Natural Polymers-based Medical Materials
School of Resource and Environmental Science
Wuhan University
Wuhan 430079, China
E-mail: zhaoze@whu.edu.cn

The ORCID identification number(s) for the author(s) of this article can be found under https://doi.org/10.1002/adma.202515030

DOI: 10.1002/adma.202515030

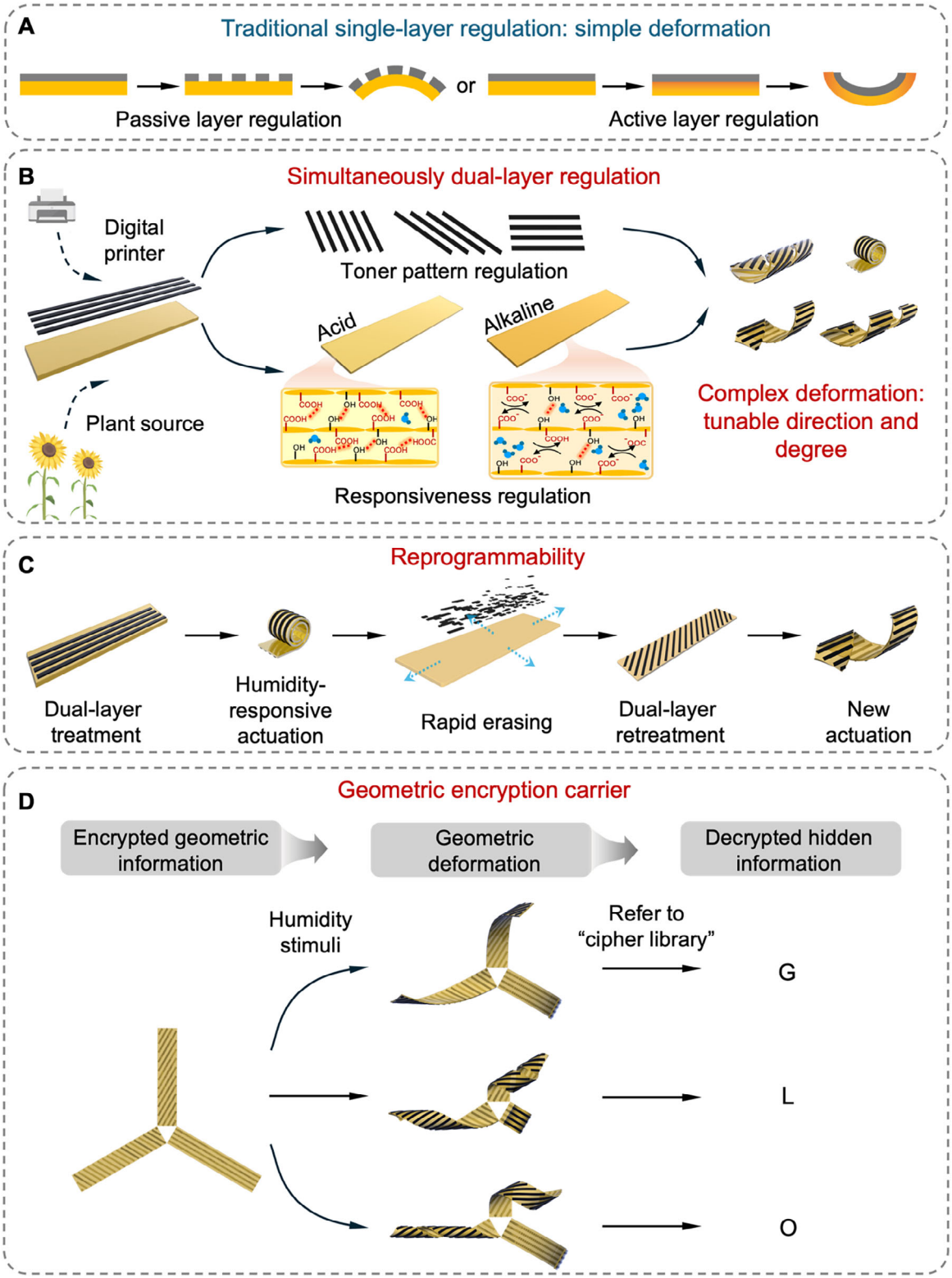

Figure 1. Schematic representation of dual-regulable and reprogrammable pollen actuators. A) Illustration of a traditional bilayer actuator with simple deformation regulated by a single layer, either passive or active layer regulation. B) Schematic illustration of dual-layer regulation of pollen-derived actuators, the simultaneous dual-layer regulation is achieved through pH treatment of the pollen paper and digital printing of toner patterns. C) Reprogrammability process of the pollen actuator. The bilayer's responsiveness can be entirely erased using a simple, aqueous-based alkaline treatment in a single step, followed by reprogramming through a new cycle of pH treatment and digital printing. D) Illustration showing the pollen actuator can be a promising candidate for 3D geometric encryption applications.

ability to fully erase and reset the programmability. Thus, a key challenge remains the development of actuators that can achieve both dual-layer regulation and complete, repeatable reconfiguration. Therefore, our pollen-based actuator emerges as a particularly compelling candidate to address these limitations.

To enable effective re-programmability in bilayer systems, both the responsiveness of the active layer and the geometric patterning of the passive layer must be independently tunable. For reprogramming the active layer, existing approaches involve the sophisticated introduction of regulable molecular structures, such as calcium-regulated thermal responsive silk-fibroin,[24] pH-responsive liquid crystalline network (LCN) with variable crosslink densities,[25] or mechanically tunable polylactic acid/carbon nanotube/polyethylene terephthalate (PLA/CNT/PET) bilayer actuators.[1] On the other hand, the tunability of geometrical patterns is related to localized regulation, such as re-designed light-responsive patterns on LCNs[26] and rewritable crosslinker patterns within the polyampholyte hydrogel.[27] However, these alternations on the active layers require responsive synthetic molecular designing and meticulous fabrication, which are time-consuming and energy-intensive. Conversely, re-patterning the passive layer generally necessitates physical disassembly and reassembly processes, which are impractical for stable, firmly adhered bilayer systems and remain rarely reported. Therefore, there is an urgent need for a bilayer actuator design that simultaneously facilitates easy and reversible programmability of dual layers through a facile, mild, and sustainable approach.

Herein, we present a pollen-based actuator that achieves unprecedented dual-layer programmability and reconfigurability through a rapid and energy-efficient "one-pot" process. Derived from natural resources, our bilayer actuator features a humidity-responsive active pollen layer whose responsiveness can be precisely modulated by pH, paired with a digitally printable passive toner layer for designable geometric patterning. Together, both layers work synergistically to modulate the degree and direction of actuation in response to humidity change (Figure 1B). Both the pollen responsiveness and toner patterns can be simultaneously erased using a mild alkaline solution, enabling a complete reset of the bilayer's programmed properties.,[28] facilitating subsequent reprogramming through repeated pH modulation and digital printing. The actuator demonstrates the highly advanced flexibility and integration of multi-modal autonomous actuation. As a proof-of-concept demonstration of the dual regulation on the degree and direction, we introduce a humidity-decoded 3D geometrical encryption carrier analogous to an encrypted binary encoding with high information capacity. The actuator can encode, transmit, and decode information symbols representing all 26 alphabet letters and a dash, thus serving as an advanced and secure platform for information communication. With straightforward, low-energy fabrication and full recyclability, this natural-material-derived bilayer actuator sets a new benchmark for reprogrammable soft actuators, offering promising opportunities for next generation of smart material systems.

2. Results and Discussion

Sources from natural plants, sunflower pollen grains (*Helianthus annuus*), we first fabricated pollen microgel suspension through two steps, organic solvent treatments and traditional soapmaking, as previously reported.[29–32] The Field Emission Scanning Electron Microscopes (FE-SEM) images of raw bee pollen grains, defatted pollen, and pollen microgel particles exhibited the spiky morphologies in Figure S1 (Supporting Information). Then, the pollen paper was obtained by drying the pollen microgel suspension in a petri dish at room temperature.[33] Subsequently, the pollen paper was treated with a pH solution as an active layer, and the passive toner pattern was digitally printed as a passive layer, obtaining the humidity-responsive bilayer actuator. To achieve an asymmetric actuation response of the bilayer actuator, the ability to asymmetrically accommodate the stimuli is crucial.[34] Here, we can simultaneously tune the asymmetric capabilities by moderating the actuation magnitude degree via pH treatment and moderating the actuation direction using digital printing, which illustrates a highly customizable strategy for achieving complex shape actuation (Figure 1B). The alkaline-treated pollen paper exhibited better hygroscopicity, absorbing more water vapor than the acid-treated paper. As a result, the alkaline-treated bilayer actuators showed more significant shape actuation, with more pronounced asymmetric deformation as the relative humidity (RH) shifted from high to low due to more substantial mechanical contraction effects. Meanwhile, the passive toner pattern and the responsiveness of the active layer can be easily erased in "one pot," allowing for a subsequent new cycle of the reprogramming process (Figure 1C). This subsequent reconfiguration cycle, combined with a new round of pH treatment and digital printing, enables a new actuation responding to RH variations. This reprogrammable and dual-regulable bilayer actuator system can be a promising candidate for transmitting encrypted information. We designed three-channel ciphers with an identical shape when not triggered by humidity to encrypt geometric information (Figure 1D). After being stimulated by humidity, they presented different geometric deformations; then, the hidden information can be decoded based on the cipher library to transmit the decrypted information.

The hygroscopicity of the active pollen layer is a critical factor in the performance of moisture-driven actuators, as it is directly influenced by the chemical functional groups present in the pollen paper. Pollen microgel particles presented pH chemo-mechanical responsiveness owing to the existence of carboxyl groups,[35] which are also exposed on the surface of as-assembled pollen papers.[28,36] The pH of pollen paper influences the protonation state of its surface functional groups, which in turn affects its water affinity and hydrogen bonding. To examine how pH alters the hygroscopic properties of pollen paper, we treated samples in solutions of pH 2, 4, 6, 8, 10, and 12, followed by drying under ambient conditions (**Figure 2A**). After pH treatment, the dry pollen papers exhibited slight shrinkage in size compared to the original dry papers (Figure S2, Supporting Information). We first characterized the moisture content after drying the pH-treated pollen papers in an ambient environment. As shown in Figure 2B, the moisture content increased progressively with higher pH levels, ranging from ≈5% of pollen papers treated at pH 2 to ≈11% for those treated at pH 12. This indicated that alkaline-treated pollen papers exhibited a greater capacity to absorb water molecules from the surrounding air. Subsequently, we hydrated pollen papers in deionized (DI) water to directly compare water affinities after different pH treatments (Figure 2C).

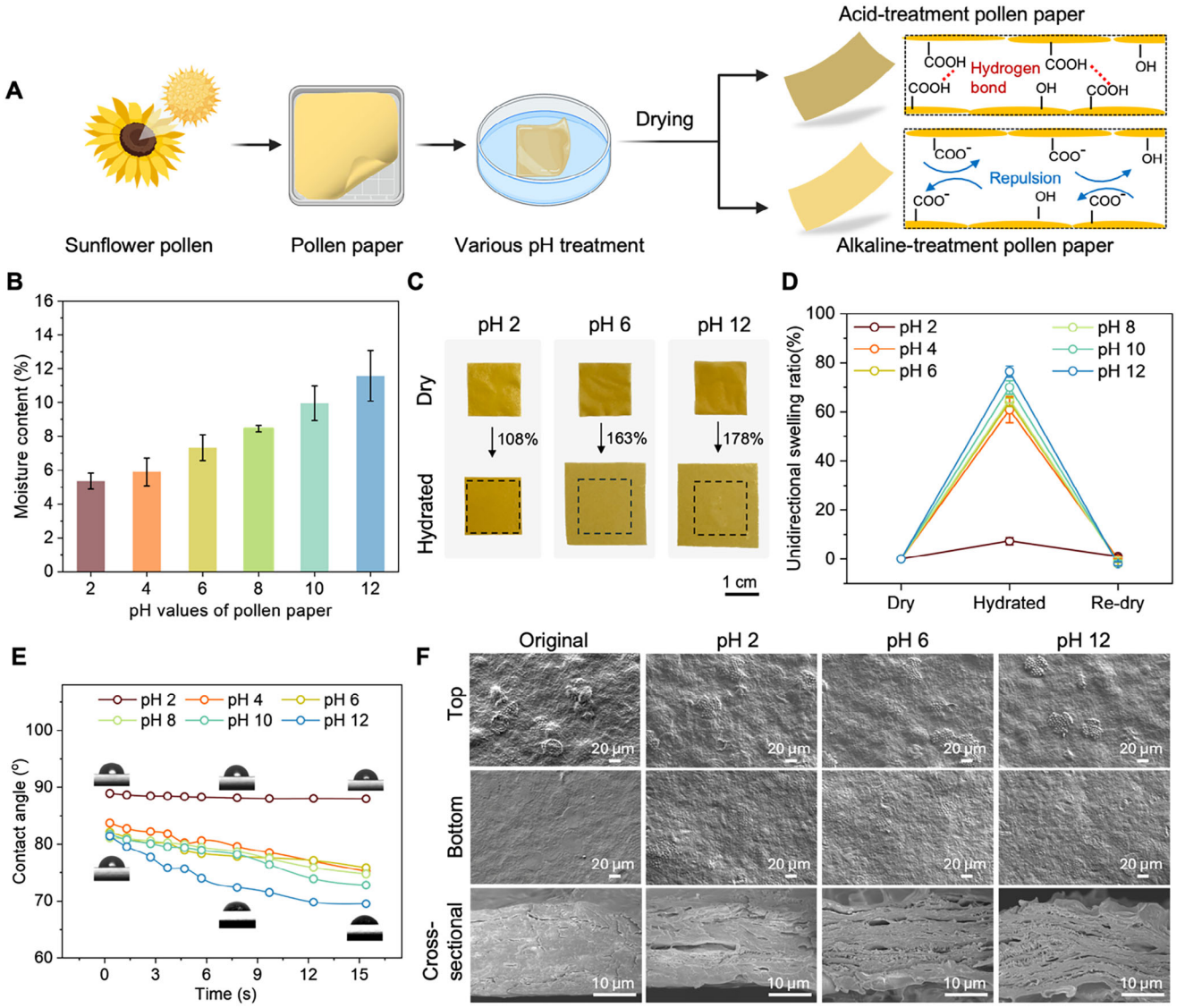

Figure 2. Comparison of the water sensitivity of pollen layers under different pH treatments. A) Schematic of the pH treatment process applied to pollen papers, illustrating the protonation and deprotonation of carboxylic acid functional groups. B) Moisture content of pollen papers following different pH treatments. C) Representative images of dry and hydrated pollen papers after exposure to various pH treatments. D) Unidirectional swelling ratio of pollen papers in dry, hydrated, and redried states after different pH treatments. E) Surface contact angles of dry pollen papers under different pH treatments. F) FE-SEM images showing the top surface, bottom surface, and cross-section of dry pollen papers after different pH levels.

It was evident that pH 2-treated pollen paper showed a slight swelling, whereas those treated at higher pH levels underwent significant expansion, reaching ≈178% of the area swelling ratio for pH 12-treated pollen paper (Figure S3, Supporting Information). The unidirectional and thickness swelling ratios were quantified for statistical analysis (Figure 2D; Figure S4, Supporting Information). The hydrated pollen papers exhibited a gradual increase in unidirectional expansion and thickness from pH 2 to pH 12 treatment, followed by a higher shrinking ratio upon further dehydration, suggesting better water vapor absorption capability of pollen papers after higher pH treatment.

The hydrophilicity ability was characterized using static water contact angle measurements, as illustrated in Figure 2E. The contact angle of pollen papers demonstrated an inverse correlation with pH values and contact time. The pollen papers treated at pH 2 exhibited an initial contact angle of 89°, slightly decreasing to 87° within 15 s. In the meantime, the contact angle of pollen papers treated at pH 12 was lower at the beginning, measuring ≈82°, and further reduced to ≈70° over an extended time. The static water drop images on the surface of pollen papers subjected to both different pH treatments and varying time intervals are provided in Figure S5 (Supporting Information). Notably, alkali-treated pollen papers displayed significantly greater water affinity than their acid-treated counterparts. Moreover, we also compared the top surface, bottom surface, and cross-sectional surface of the original pollen paper and various pH-treated pollen papers through FE-SEM images (Figure 2F). It was observed that the newly fabricated original pollen paper had

a very smooth bottom surface and a rough top surface. However, the acid- and alkaline-treated papers possessed rough surfaces on the top and bottom sides (Figure S6, Supporting Information). The surface microroughness of pollen papers contributes to the interlayer adhesion and the integrity of bilayers. Thus, the original pollen paper can only be printed on rough top surfaces. However, pH-treated pollen papers enable digital printing on both rough surfaces for digital printing, significantly expanding their functional versatility. Besides, original pollen papers demonstrated denser and more compact cross-sectional structures than pH-treated samples. Although the acid-treated pollen exhibited dense cross-sectional structures, the alkali-treated papers showed more pronounced gaps and pores between lamellar structures, which resulted from molecule aggregations among pollen particles (Figure S7, Supporting Information).

The macroscopic deformation of bilayer actuators arises from the strain mismatch between active and passive layers in response to humidity changes, where the strain response of active layers plays a pivotal role. We initially characterized the mechanical properties of the active pollen layers. We first conducted uniaxial tensile tests on pollen papers subjected to various pH treatments in high RH (≈60%) and low RH (≈20%) environments. The stress-strain curve of pollen papers obtained under RH 60% is presented in **Figure 3**A. The failure strain of pollen papers increased markedly as pH decreased, ranging from ≈15% at higher pH levels to 65% at pH 2. In contrast, the ultimate breaking strength remained relatively constant at ≈11.5 MPa across all samples. Additionally, Young's modulus, determined from the initial linear region of the stress-strain curves, showed an increasing trend with decreasing pH, reaching ≈225 MPa for pollen papers treated at pH 2 (Figure 3B). When RH was reduced to 20%, both the failure strain and ultimate breaking strength of pollen papers decreased compared to their values at RH 60%. At RH 20%, the failure strain and Young's modulus increased with decreasing pH (Figure 3C,D), while the ultimate breaking strength fluctuated, rising from ≈3 MPa at pH 12 to ≈8 MPa at pH 2. These findings indicate that pollen papers treated in alkaline conditions are highly sensitive to humidity changes, as evidenced by the significant drop in ultimate breaking strength when RH decreased from 60% to 20%.

To further investigate the shape evolution during the hygroscopic deformation, the dynamic mechanical response of the active pollen papers was analyzed under varying RH conditions. The unidirectional strain of different pollen papers was measured over time without external stress or force as RH altered (Figure 3E,F), with real-time RH fluctuations shown in Figure S8 (Supporting Information). When RH dropped from ≈60% to 20% over 10 min, hygroscopic shrinkage in the length direction increased with higher pH levels. The pH 2-treated pollen papers exhibited a unidirectional shrinkage strain of ≈0.2% while RH decreased from 60% to 20%, while pH 12-treated samples showed a larger shrinkage strain, ≈1.5% when RH was reduced to 20%. This greater contraction in alkaline-treated samples is attributed to their higher initial water content at high RH, leading to more significant moisture loss during dehydration.

To better understand the mechanism of pH regulation, Fourier transform infrared (FTIR) spectroscopy was used to characterize the pollen papers treated with different pH levels. As shown in Figure 3G, the peak at 1706–1716 cm^{-1} corresponding to the protonated carboxyl group decreased as pH increased. In contrast, the peaks ≈1653–1663 and 1435–1489 cm^{-1}, corresponding to asymmetric and symmetrical stretching of carboxylate groups (—COO^-), were significantly enhanced in pollen papers after alkali treatment.[37,38] This indicated the formation of carboxylate groups (—COO^-) resulting from the deprotonation of carboxylic acids (—COOH) as pH increased.[37,38] The increased presence of carboxylate groups implies a corresponding enhancement in electrostatic repulsion forces between these negatively charged moieties. To further demonstrate the deprotonation of pollen papers, the zeta potential of different pH-treated pollen papers in aqueous solution was measured, as shown in Figure S9 (Supporting Information). With an increase in pH values from 2 to 12, the zeta potential of pollen papers decreased from ≈−18 to ≈−38 mV, exhibiting a similar tendency in zeta potential change to that of dispersed pollen microgels. But the zeta potential of pollen microgels increased from pH 10 to 12, because they were measured in pH 12 solutions, which induced a high ion concentration that interfered with the zeta potential. Additionally, the peak width of hydroxyl (-OH) stretching at 3000–3700 cm^{-1} from alkali-treated pollen papers was much more expansive than acid-treated samples (Figure S10A, Supporting Information). This suggested the presence of nonuniform hydrogen bonds in alkaline-treated samples, owing to the accumulation of water molecules within pollen papers.[39] To further demonstrate the impact of water accumulation in pollen papers upon different pH treatments, the FTIR spectra of pollen papers were normalized and subjected to subtractions (RH 60% minus RH 20%), as shown in Figure S10B (Supporting Information). Under high RH, the peak region at 3000–3700 cm^{-1} expanded after alkaline treatment, indicating greater water absorption in alkali-treated samples with higher water affinity. Moreover, the peak intensity at 1640 cm^{-1}, associated with the O—H bond in water molecules,[39,40] amplified and became more prominent after alkali treatment, with a blue shift observed from 1651 to 1636 cm^{-1} as the pH increased from 2 to 12. These findings indicate that acid-treated pollen papers, with lower water content, formed more uniform hydrogen bonds between pollen particles, leading to a higher Young's modulus, as previously discussed. In contrast, in alkali-treated pollen papers, deprotonated carboxyl groups generated stronger electrostatic repulsion, promoting water cluster accumulation. This disrupted the uniform hydrogen bonding between pollen particles, as illustrated in Figure 3H.

To systematically investigate the deformation behaviors of the pollen bilayer actuators subjected to the change of RH, a series of actuators was fabricated, consisting of various passive layers (toner patterns) and active layers (pollen papers). These bilayer actuators were then tailored into rectangular ribbons for analysis (**Figure 4**A). The micromorphologies of the surface and cross-section of the bilayer actuator are displayed in Figure 4B,C. It was observed that the toner printed on the pollen paper formed a fused coating layer, which was well-adhered along the contour of the surface of the pollen layer. The thickness of the toner layer was ≈15 µm, and the pollen layer was ≈30 µm. Furthermore, statistical analysis was performed to evaluate the influence of pH treatments and toner pattern orientations on the shape deformation behaviors of the actuators. Figure 4D schematically illustrates the coiling geometry parameters corresponding to the shape configurations of pollen ribbons, including toner pattern

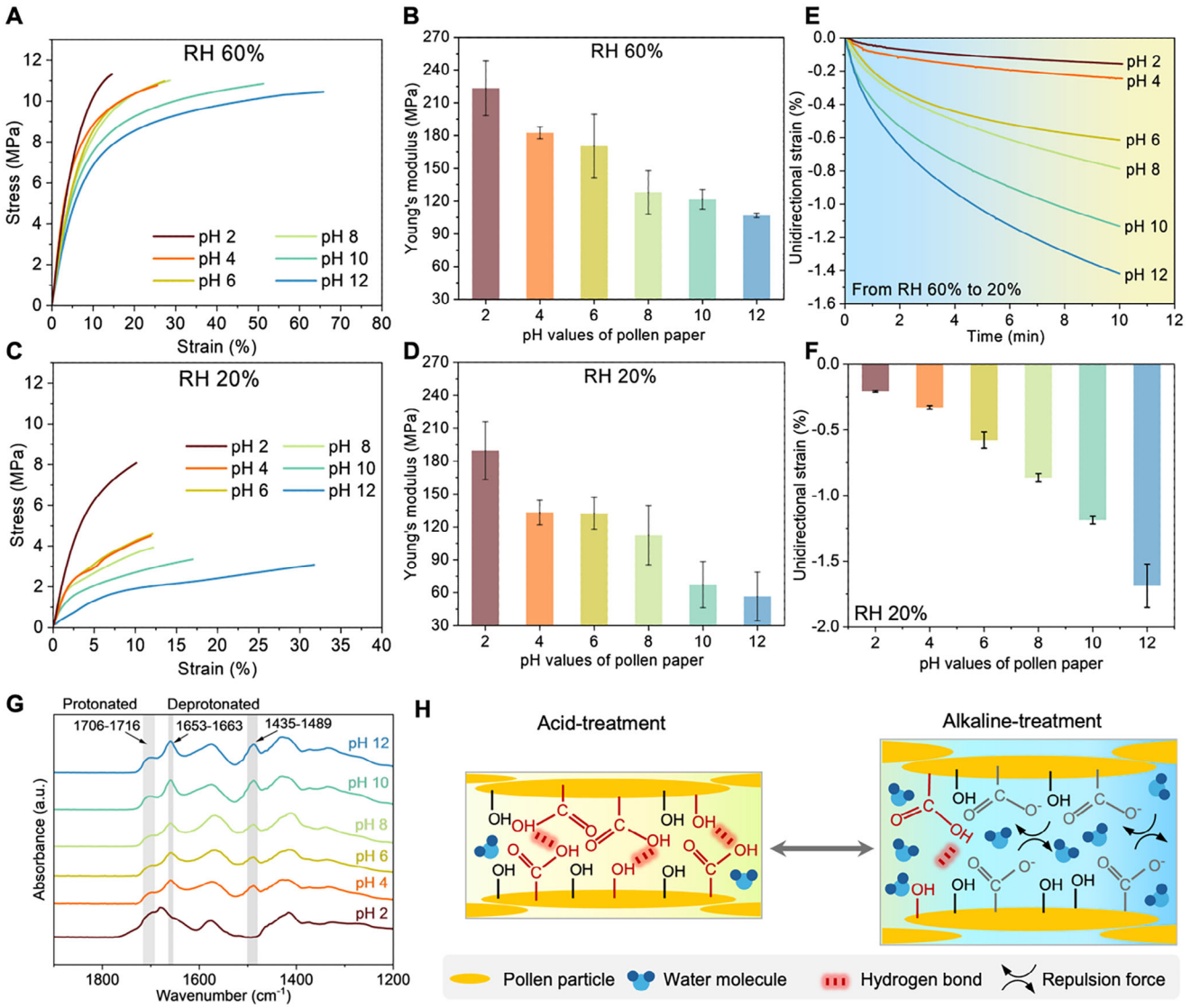

Figure 3. Mechanical properties and mechanistic analysis of pollen papers under different pH treatments. A) Stress-strain curves of pollen papers treated at various pH levels at RH 60%. B) Young's modulus of pollen papers following different pH treatments at RH 60%. C) Stress-strain curves of pollen papers subjected to different pH treatments at RH 20%. D) Young's modulus of pollen papers following different pH treatments at RH 20%. E) Time-dependent shrinkage behavior of pollen papers after different pH treatments, measured as uniaxial strain under zero applied stress, upon reducing RH from 60% to 20%. F) Shrinkage strain values of the pollen papers after different pH treatments upon reducing RH from 60% to 20% under zero applied stress. G) FTIR spectra of pollen papers treated at various pH levels, highlighting chemical modifications. H) Schematic representation of internal chemical bonding and water molecule distribution in pollen papers following different pH treatments.

orientation angle (θ), coiled cylinder diameter, and pitch, defined as the distance between two consecutive turns along the coiling axis.[31] The shape configuration behaviors were evaluated using four distinct toner patterns, including 30°, 45°, 60°, and 90°, and pollen papers subjected to various pH treatments, including pH 2, 4, 6, 8, 10, and 12.

The pollen bilayer ribbons were hung in a chamber to observe the shape evolution processes in response to a reduction of RH from ≈60% to ≈20%. To investigate the influence of the toner pattern layers, the bilayer actuators consisting of four different toner patterns (30°, 45°, 60°, and 90°, respectively) and the two different pH-treated pollen active layers (pH 2 and pH 12) presented various shape deformation behaviors in Figure 4E,F, and Figure S11 (Supporting Information). The geometric orientation of pattern layers could impact the coiling curvature and axial direction of the bilayer actuators. When the pattern was printed parallel to the long side of pollen ribbons (θ = 90°), the bilayer actuator coiled along the long axis and displayed a ring shape. When the pattern orientation angle (θ) changed between 90° to 0°, the sample presented a helical morphology, where the helically coiled axis angle between the long axis of pollen ribbons corresponds to the pattern orientation angle and the longer helices formed at lower values of θ. The effects of the toner orientation angles (θ) on the humidity-responsive shape evolution of actuators are

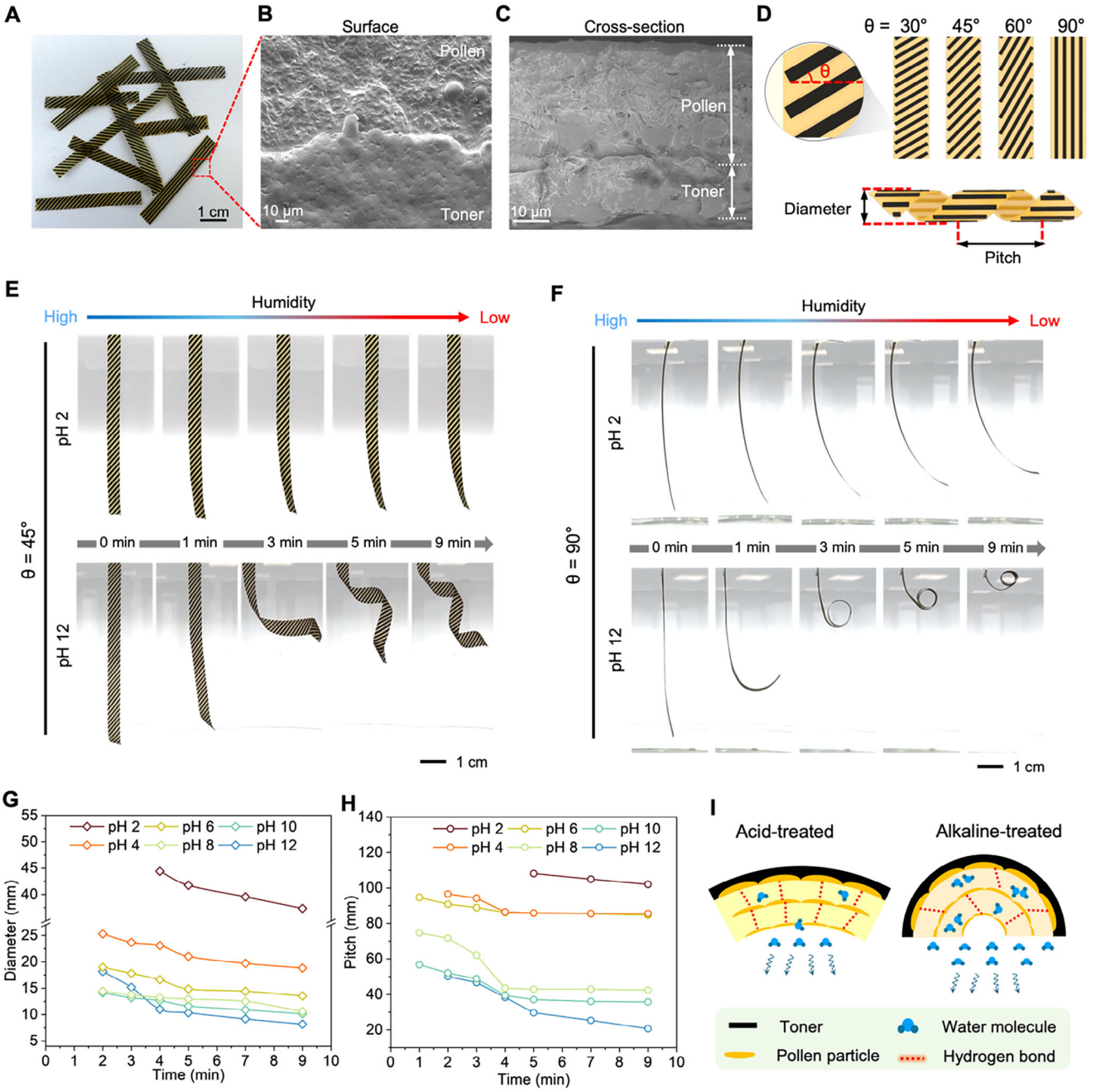

Figure 4. Self-coiling morphology of pollen actuators regulated by toner pattern in response to RH changes. A.) Images of bilayer pollen actuator ribbons. B) FE-SEM images of the surface morphology of bilayer pollen actuators. C) FE-SEM images of the cross-sectional structure of bilayer pollen actuators. D) Schematic representation of the coiling geometry and nomenclature of patterned bilayer ribbons. E) Programmed self-coiling response of bilayer actuators treated at pH 12 and pH 2 with a pattern orientation angle (θ) of 45°, as RH decreases from ≈60% to ≈20%. F) Programmed self-coiling response of bilayer actuators treated at pH 12 and pH 2 with $\theta = 90°$, as RH decreases from ≈60% to ≈20%. G,H) Time-dependent evolution of coiling diameter and pitch for pollen actuators with different pH treatments when $\theta = 45°$. I) Schematic representation of the internal microarchitecture of acid- and alkali-treated pollen actuators when RH is reduced to 20%.

statistically illustrated in Figure S12 (Supporting Information). It was detected that the diameter and pitch size decreased with the increase of orientation angles (θ).

On the other hand, the pH conditions of the active pollen layers could influence the deformation degree of the actuators. Under the same toner pattern, the bilayer actuators exhibited tighter helices and more successive coiling turns with increased pH values of pollen substrate layers (Figure S13 and Movies S1–S6, Supporting Information). Based on the pattern line angle, $\theta = 45°$, we statistically analyzed the coiling diameter and pitch changes as a function of time, where both the diameter and pitch reduced with the increase of pH levels and reached a steady state within

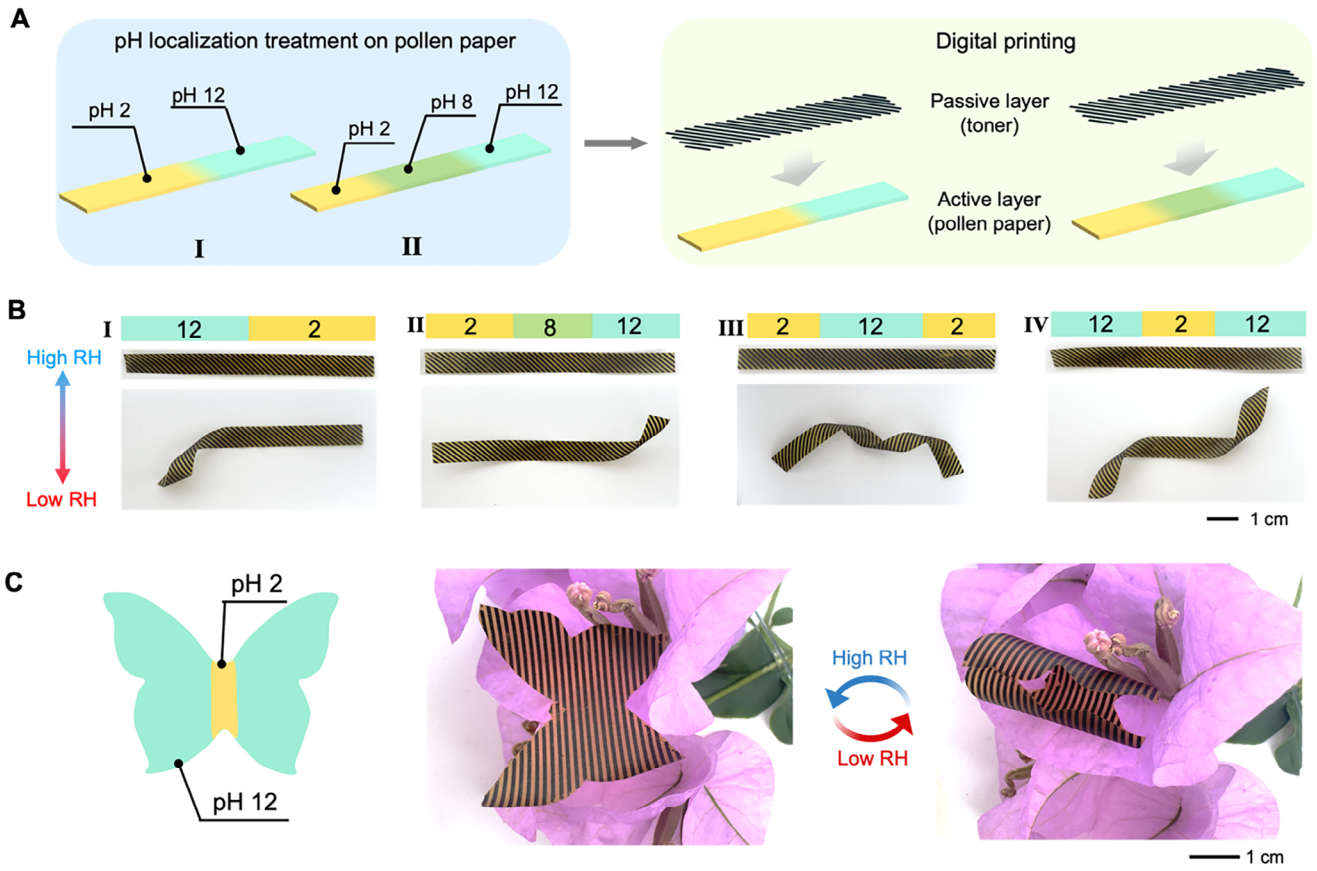

Figure 5. pH localization treatment on patterned bilayer pollen actuators enabled complex hygromorphic deformation. A) The fabrication process of the pH localization treatment was applied to active pollen papers, followed by digital printing with a uniform pattern. B) The 3D configurations of the bilayer pollen actuators exhibited multiple coiling modes in response to RH changes from ≈60% to ≈20%. Different regions of the pollen strips were treated with distinct pH values and printed with the same patterns (light blue color: pH 12, yellow color: pH 2, green color: pH 8). C) Top-view image of a bilayer pollen butterfly structure, showing wing fluttering behaviors in response to RH changes from ≈60% to ≈20%.

7 min, as presented in Figure 4G,H. To more precisely quantify the deformation procedure of the actuator, we measured the specific bending curvature of the actuators pretreated under various pH values during both the actuation and recovery process, with the change of RH between 60% and 20%, as displayed in Figure S14A (Supporting Information). It was found that with an increase in treated pH values, the bending curvature increased from ≈0.1 cm^{-1} at pH 2 to ≈0.7 cm^{-1} at pH 12, accompanied by a corresponding acceleration in response speed. Moreover, we also further precisely analyzed the impact of pattern orientation (θ) on the folding angles (α), as illustrated in Figure S14B (Supporting Information). When the pattern orientation angle (θ) was 0°, the folding angle was ≈152°, and as θ was raised to higher values until 90°, the folding angle steadily decreased to 0°. We also compared the response speed and curvature of our work with those of other actuators (Table S2, Supporting Information). Our work exhibited greater deformation behaviors with higher curvatures, ranging from 0.036 to 0.28 cm^{-1}, compared to other actuators, although our speed was not that fast, ranging from 0.15 to 1.04 °/s. The combination of pH treatment and strategic toner pattern orientation enables a dual-level regulation of the coiling deformation, facilitating easily customizable shape transformation dynamics in response to environmental humidity. As previously discussed, pollen layers treated under alkaline conditions exhibited superior hygroscopic properties compared to those treated with acid. The enhanced hygroscopicity facilitated more significant water molecular release, resulting in more pronounced shrinkage as RH decreased. It led to a more considerable strain mismatch between the pollen layer and the mechanically constraining toner layer, displaying more distinguishable shape deformations, as depicted in Figure 4I.

The pH regulation of the active layers was not only limited to the entire intact layer but also could be achieved in specific regions, which has rarely been reported in conventional actuators. This capability enhanced the versatility of the bilayer actuator, achieving various locomotion actions under the same pattern of the toner layer on the same bilayer actuator, which introduced a novel approach to actuator design. To demonstrate this kind of multi-modal configuration on the pollen bilayer actuators, localized pH treatment was applied to specific areas of the substrate pollen active layers. As shown in **Figure** 5A, different regions of pollen ribbons were treated under varying pH conditions (pH 2, 8, and 12). The same toner patterns ($\theta = 45°$) were then printed onto the treated pollen strips to form bilayer actuators, which exhibited no significant differences at the initial state under RH 60%. With the RH decreased to 20%, various pH

localized treatments resulted in different deformation degrees, although these same patterns shared an identical curvature axis angle for shape deformation, as illustrated in Figure 5B. When the RH decreased from ≈60% to 20%, the areas treated with pH 2 presented only slight curvature, whereas regions treated with pH 12 formed helices with multiple consecutive turns. Meanwhile, the pH 8-treated pollen ribbons displayed helical curvatures limited to half turns. These diverse deformation modes were integrated into a single pollen actuator, enabling great flexibility and variety in shape configurations.

Moreover, leveraging its excellent printability and tunability, the pollen bilayer actuator can mimic the motion of organisms such as butterflies in response to changes in humidity (Figure 5C). Following regional processing, digital printing, and shape cutting, the butterfly's body was treated with pH 2, while the wing areas were treated with pH 12. As the RH decreased from 60% to 20%, the pollen butterfly exhibited wing-flapping motions atop a flower. These results highlight the incredible versatility and tunability of the dual-regulable pollen bilayer actuator in facilitating 2D-to-3D structural transformations driven by humidity changes.

pH-treated pollen papers exhibited extensive swelling in DI water under hydrated conditions, with the swelling ratio increasing at higher pH values. Based on this observation, we hypothesized that alkaline immersion could also induce swelling on the active pollen layer of bilayer actuators, potentially leading to the disintegration and detachment of the toner layer and enabling the re-programmability of the bilayer pollen actuators. As shown in **Figure 6**A, when the pollen bilayer actuator was immersed in a basic solution, it initially curled up within a short time due to the water absorption in the active pollen layer, resulting in asymmetric actuation. With continued swelling, the pollen paper expanded further, causing the toner layer to disintegrate. Within 24 s, the toner fragments began to detach, and genital agitation facilitated their removal. Complete toner disassembly occurred within ≈2 min. To reprogram the actuators, we developed a simple and mild process, illustrated in Figure 6B. The toner pattern (passive layer) and the hygroscopic responsiveness of the active pollen layer were effectively removed in a "one-pot" basic solution with gentle shaking, followed by a water rinse. The recycled pollen paper was then reconditioned in a new pH solution and prepared for fresh digital printing, enabling reconfiguration. This method is efficient, environmentally friendly, and operates under ambient conditions with minimal processing steps. The optical microscopic images were taken to record the recycling process of the pollen actuator, which demonstrated the high-resolution pattern of the toner after being reprinted onto the pollen papers, as shown in Figure S15A (Supporting Information). Initially, the toner layer firmly adhered to the surface of the pollen layer. Subsequent immersion in an alkaline solution and water caused the pollen paper to swell and the toner layer to disintegrate and detach. After pH adjustment and air drying of the pollen layer, the roughness of the pollen paper recovered, and the new pattern layer was reattached to the surface via new digital printing, successfully obtaining a high-resolution pollen actuator (Figure S15B, Supporting Information).

We subjected the pollen papers to multiple cycles of basic/pH solution treatments combined with repeated printing processes. The hygroscopic rein the change of RH. Initially, the pollen paper treated with pH 12 was printed with toner pattern lines oriented at 60°, resulting in helical coiling behaviors as a reduction of RH. Subsequently, the first recycled pollen actuators, treated with pH 2 and printed with toner patterns at 90°, exhibited slight bending (Figure 6C). After that, the second recycled pollen actuators presented stable helical deformations with multiple successive turns, while the third recycled actuators, treated with pH 6, displayed mild helical curvatures as RH decreased. Additionally, we evaluated the mechanical properties and changes in unidirectional shrinkage strain of pollen papers during 10 cycles of pH treatment between pH 12 and pH 2, as shown in Figure 6D,E. There were no obvious changes in both Young's modulus and unidirectional strain after 10 cycles. We also compared the detailed dynamic unidirectional strain changes of the original (0) cycle and the 10th cycle as a function of time in response to RH changes between 60% and 20% (Figure S16, Supporting Information). Remarkably, the response speed and unidirectional strain didn't present significant changes after 10 cycles. Therefore, even after 10 cycles of recycling and reprinting, the pollen paper maintained consistent shape deformation behaviors with those of newly fabricated pollen actuators. Moreover, we have compared our pollen-based actuators with other programmable stimulus-responsive actuators, such as IR light,[2,9,13] electrical,[41] and temperature-responsive actuators,[2,23] as shown in Table S3 (Supporting Information). Most responsive materials relied on programming via a single layer, facing significant limitations in achieving reconfigurability. Although the PNIPAM/PVA/BISS[2] and LCN-based systems[25] have demonstrated certain degrees of re-programmability, their reconfigurations were constrained by the initially programmed architecture and cannot be fully reset. In contrast, our pollen-derived actuators, which leverage the inherent properties of toner segments and pollen papers, enable a complete decoupling and reprogramming of both layers, resulting in entirely new actuator deformations. This allows the actuator to be entirely reprogrammed and reused as a new device, offering a level of functional adaptability that is difficult to achieve in conventional systems.

Most actuators responsive to external stimuli are designed with single-layer regulation, while dual-layer modulation remains largely underexplored. By employing multi-modal autonomous actuation strategies, dual-layer systems can surpass the functional constraints of conventional designs, enabling the development of complex architectures with greater adaptability and multifunctionality. In our pollen-based bilayer system, samples with identical toner patterns exhibited comparable macroscopic properties, such as color, thickness, and surface texture, under ambient conditions (60% RH), confirming structural consistency prior to actuation. However, reducing the relative humidity from 60% to 20% induced distinct shape transformations, driven by molecular-level differences in the chemical properties of the active pollen layers. This dual-layer regulation and re-programmability unlock advanced applications such as encrypted information storage and transmission capabilities that are difficult to realize with single-layer systems. Furthermore, the combination of tunable active layer chemistry and programmable passive layer patterning enables the development of independent multi-channel encryption systems with high information density. As a proof of concept, a three-channel information

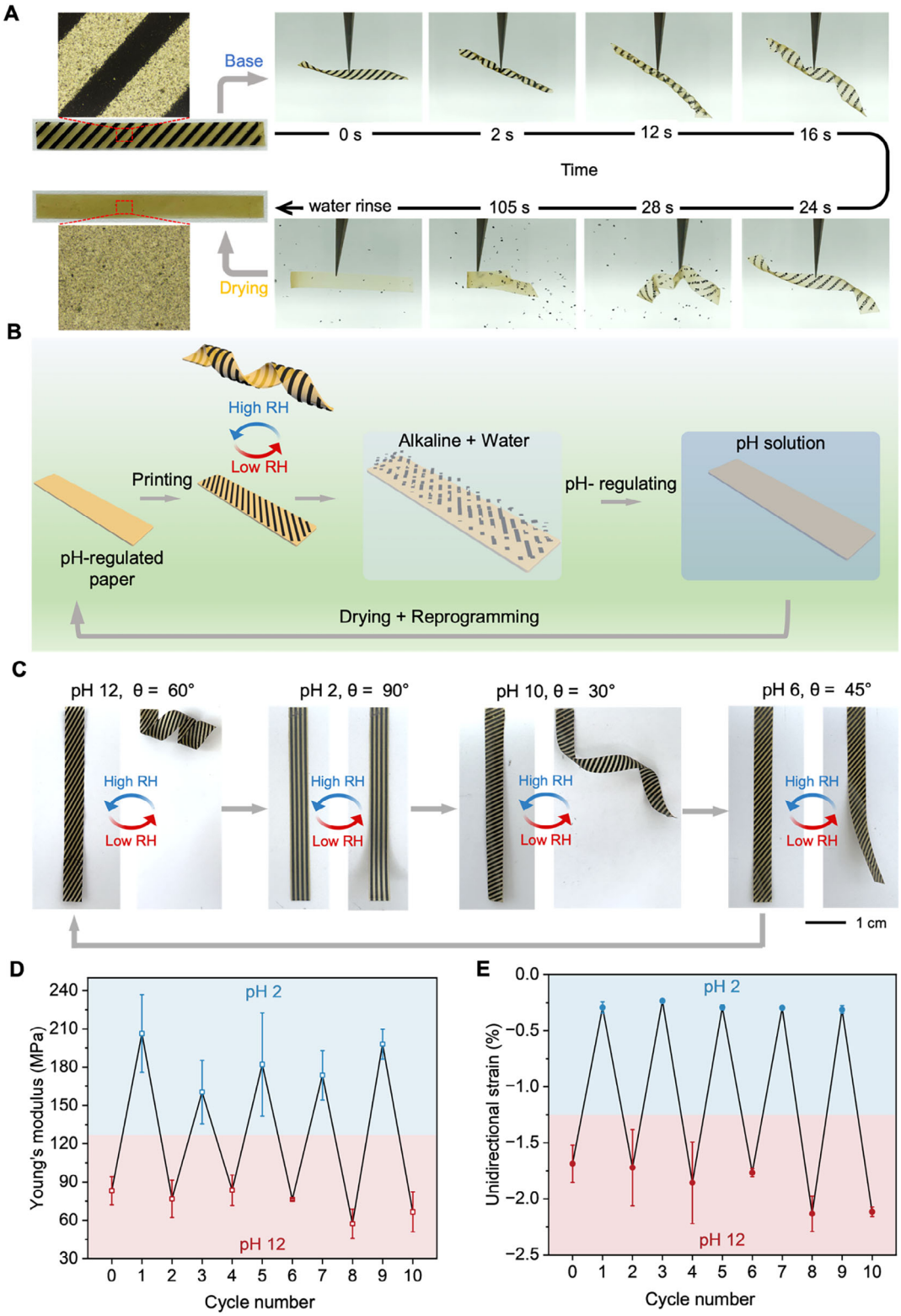

Figure 6. Re-programmability of bilayer pollen actuators. A) Toner pattern erasing on bilayer pollen actuators after alkaline and water washing. B) Schematic illustration of the recycled and reprogramming process of the dual-regulable bilayer pollen actuators. C) The 3D reconfiguration of the bilayer pollen actuators, regulated by various ink patterns and pH treatments in response to RH, changed from ≈60% to ≈20%. D) Cyclic testing of the Young's modulus of pollen paper treated between pH 12 and pH 2 for 10 cycles. E) Cyclic testing of the shrinkage strain of pollen paper treated between pH 12 and pH 2 for 10 cycles upon reducing RH from 60% to 20% under zero applied stress.

cipher system was developed using three pollen actuator ribbons to demonstrate encrypted information encoding, decryption, and transmission. The system encodes data through shape deformations triggered by humidity changes, illustrating the potential of dual-regulated actuators for secure, stimuli-responsive communication. Each of the three pollen ribbons consists of an active pollen layer treated at different pH levels and a passive toner pattern layer, as illustrated in **Figure 7**. The ribbons are designed with specific pattern orientation angles: 30° (*z*-axis), 60° (*y*-axis), and 90° (*x*-axis) (Figure 7A-I).

Using this principle, we created a three-channel cipher library that maps 26 letters and one dash (a total of 27 symbols) based on the distinct deformation patterns (Figure 7A-II). Each letter corresponds to a unique combination of deformations from the three actuator ribbons when exposed to humidity reduction. The encryption and decryption processes are shown in Figure 7A-III. Initially, at RH 60%, the two cipher systems appear identical to the naked eye, with their ribbons oriented at 30°, 60°, and 90° along the z-axis, y-axis, and x-axis, respectively. As RH decreases, the ribbons undergo distinct shape transformations. For example, in the left system, the *z*-axis ribbon forms a single helix, the *y*-axis ribbon coils multiple times, and the *x*-axis ribbon bends into several turns. This deformation pattern corresponds to the coordinate (z_2, y_3, x_3) in the cipher library, revealing the letter "L." Similarly, the right-side cipher system deforms into (z_1, y_1, x_1), which corresponds to the letter "G." This three-channel geometrical encryption system provides a novel, humidity-responsive approach for secure information storage and transmission.

Leveraging the design of the geometrical encryption cipher system, pollen actuator ribbons were developed to enable information encryption under high RH conditions and decryption under low RH conditions. An identical toner pattern design was applied between pollen ribbon systems, while the bottom pollen paper was treated with different pH levels (pH 2, pH 6, and pH 12) to achieve diverse functional capabilities. Subsequently, decryption was accomplished by inducing distinct shape deformation as RH decreased, effectively delivering the encoded messages through the geometrical encryption cipher system. It can not only transmit simple information, such as a single letter of the alphabet, but also provide more complex data, such as entire words, as shown in Figure 7B. Specifically, four systems of pollen actuators with different pH-treated pollen ribbons were designed and exhibited negligible differences under high RH for storing encryption information. Upon a reduction of RH, the pollen ribbon systems revealed a four-letter word, "LOVE." To evaluate the decoding accuracy of our geometrical encryption cipher system, we selected 30 participants to independently decode 4 letters each, resulting in a total of 120 decoding processes. To ensure the universality and usability of the shape encryption system, the participants we chose were from diverse backgrounds, ages, majors, and jobs, as shown in Figure S17A (Supporting Information). After collecting all the decoding results, the accuracy was analyzed, which can reach over 96% (Figure S17B, Supporting Information). This demonstrated that our shape encryption system could be suitable for individuals from diverse majors, age groups, and occupations. This innovative approach represents the first demonstration of a natural pollen-based reprogrammable multichannel encryption system, which reveals the hidden information through 3D geometrical deformation upon humidity stimuli. It offers multiple actuation states to convey distinct information and holds significant practical potential to enhance information security.

3. Conclusion

In summary, dual-layer, regulable, and reprogrammable natural pollen-based bilayer actuators with pronounced hygroscopic responsiveness were demonstrated and achieved through a straightforward, mild, and scalable process. The pollen actuator was programmed by the top passive toner pattern layer to regulate actuation directions in response to RH change via an effective digital printing process. Meanwhile, it was also configured by regulating the water affinity of the bottom active pollen layer via various pH treatments to achieve control of the deformation degree. Besides, our pollen actuator obtains the ability for partial region regulation, which introduces a novel approach to multi-modal actuator design. Moreover, the pollen actuator demonstrates re-programmability through an eco-friendly, rapid, and simple mild process. It enables the complete erasing of the passive toner layer and responsiveness of the active pollen layer via "one pot" treatment, which also facilitates the subsequent pH retreatment on pollen paper, eliminating the need for additional energy-intensive processes. Furthermore, these unique properties of the bilayer pollen actuator highlight its potential as a geometrical encryption cipher, similar to an encrypted binary encoding, offering innovative applications in information security and data protection.

Although the conventional definition of 4D printing is based on additive manufacturing (AM), we can consider it as an extensive concept to classify our pollen-based actuator as 4D printing because we have employed stacked and additively deposited dual layers together, which subsequently evolve into a responsive 3D morphology under humidity. Superior to conventional 4D printing, the pollen-based actuator integrates complex actuation capabilities with full re-programmability and reusability, which emerges as a promising candidate for environment-interactive multifunctional applications and contributes to environmentally sustainable information security. Regarding the sources from natural pollen materials and recyclable manufacturing process, we treat this actuator fabrication system as conditional environmental sustainability. To further demonstrate the sustainable platform, future work may explore a formal life-cycle assessment (LCA), evaluate the scalability and availability for seasonal mass production and collection, and verify the complete biodegradation of the whole device. Overall, based on the expanded 4D printing concept, this reprogrammable pollen-based actuator enables secure, environmentally interactive, encrypted device functionalities and broadens the avenues for sustainable smart devices.

4. Experiment Section

Pollen Paper Preparation: The sunflower pollen paper was fabricated through a multi-step procedure, including defatting pollen, pollen microgel preparation, and paper forms, following previously reported methods.[29,30] Initially, 500 g of raw bee pollen (Helianthus annuus, Shaanxi GTL Biotech Co., Ltd, Xi'an, Shaanxi, China) was suspended and subsequently treated with 1L of deionized (DI) water (50 °C, 2 h, 800 rpm),

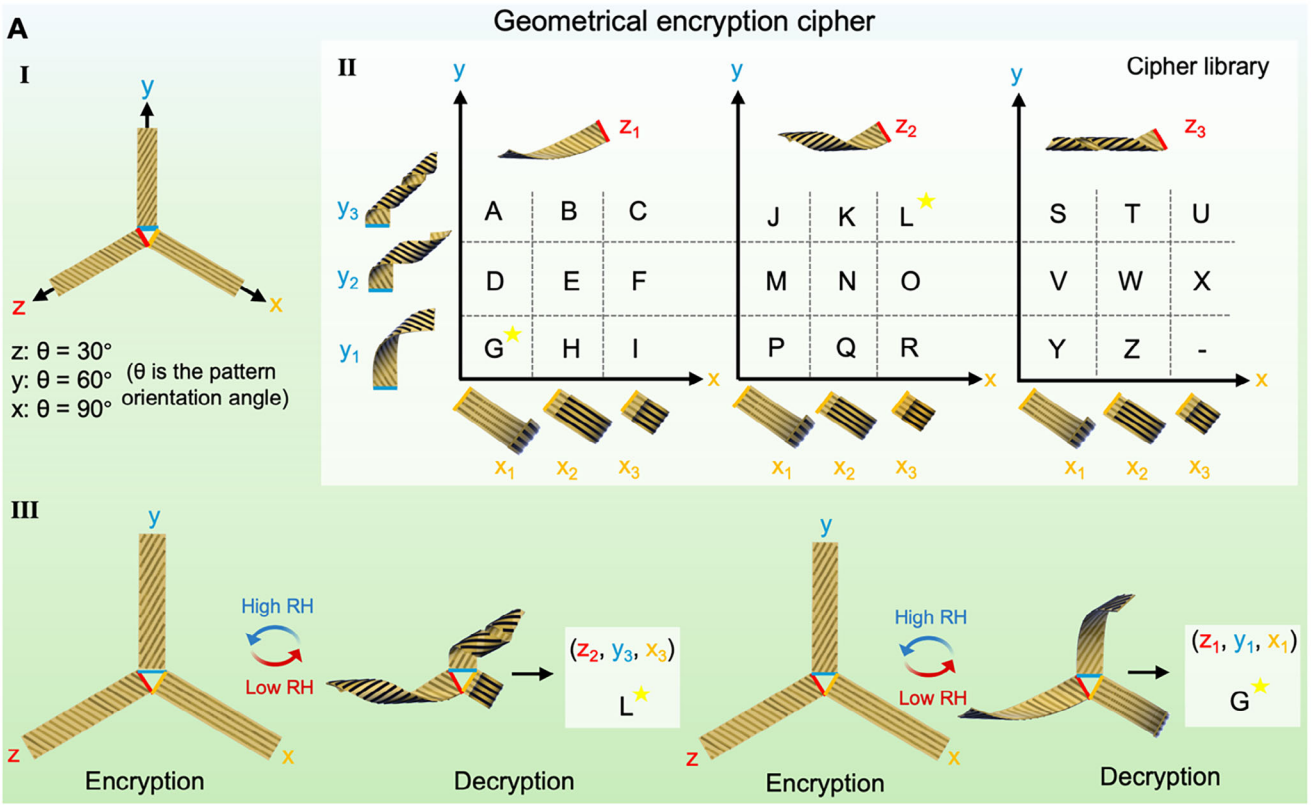

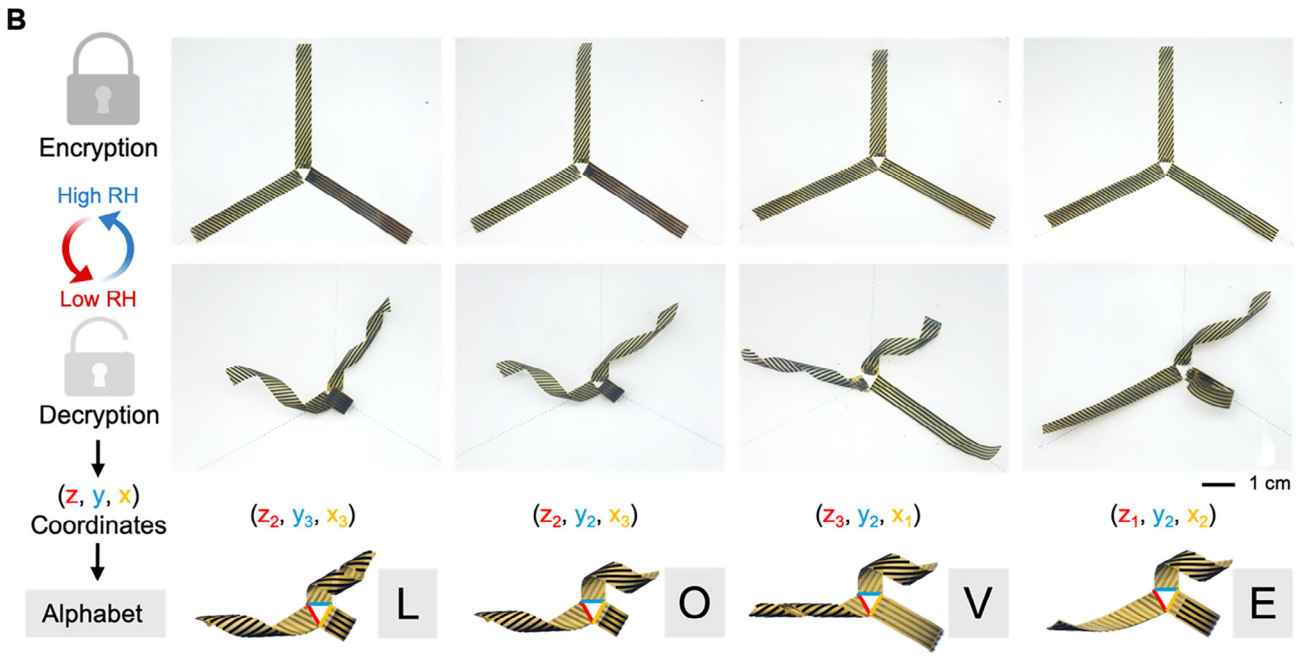

Figure 7. Applications of the bilayer pollen actuators. A) Schematic illustrations of performance and applications of bilayer pollen actuators as three-channel 3D geometrical encryption ciphers. I) The toner pattern design of the three-channel information cipher system. II) The alphabetic letters were arranged within the three-channel cipher library. III) The encryption and decryption of the three-channel shape information cipher system. B) The 3D configurations of the information encryption and decryption process of the bilayer pollen actuator ribbons triggered by RH decreased from ≈60% to ≈20%.

1L of acetone (3 h, 800 rpm), 1L of diethyl ether (2 h, 800 rpm) for 2 times and 1L of diethyl ether (12 h, 800 rpm). All the organic solvents were removed through vacuum filtration and dried overnight, resulting in the defatted pollen. For microgel preparation, 20 g of the defatted pollen was refluxed in 200 mL of 10 wt.% potassium hydroxide (KOH) with continuous stirring (80 °C, 2 h, 800 rpm), filtered through a 30 µm mesh, and washed with fresh KOH solution until clear. The samples were further incubated in KOH to promote de-esterification (80 °C, 24 h), then neutralization with DI water through a 35 µm mesh until a pH of ≈7.5 was reached, forming microgels. Ultimately, the pollen microgels were cast into a petri dish for air-drying under an ambient environment to obtain the pollen paper.

pH Regulation of Pollen Paper: The acid buffer solution was prepared by dissolving 10 mL of 2 M hydrochloric (HCl) solution in DI water (100 mL), followed by adjusting and titrating to the desired pH values (pH 2, 4, 6) with HCl and KOH solution. Meanwhile, the alkaline buffer solution was prepared by dissolving 5 g of KOH pellets in DI water (100 mL) and titrating to the desired pH values (pH 8, 10, 12) with KOH and HCl solution. Then, the original pollen paper was immersed in buffer solutions with different pH values for 2 h. After that, the treated pollen papers were taken out for air-drying under an ambient environment for further testing.

Digital Printing of Pollen Paper: The toner patterns were prepared using AutoCAD 2018 and printed on pollen papers through monochrome printing with HP LaserJet Pro MFP M428fdn (HP Inc.) at a resolution of 1200 dpi. Then, the toner-patterned pollen papers were tailored into desired simple shapes.

Pollen Paper Characterization: The moisture content of pollen paper was measured by a thermogravimetric analyzer (TGA Q500) with a temperature ramp of 5.00 °C min^{-1} to 120.00 °C, and the moisture content was calculated based on the mass loss at ≈100 °C. Optical photographs and videos were captured via iPhone 14 ProMax (4K resolution). The water contact angles of pollen samples were measured by a tensiometer (Attension Theta, BiolinScientific). The water drop shapes and contact angles were analyzed via One Attension software. The SEM images of surface microstructures and cross-sectional structures were obtained through a JSM-7600F Schottky field-emission scanning electron microscope (JEOL, Tokyo, Japan) under an accelerating voltage of 5 kV. The Fourier transform infrared (FTIR) spectra of pollen samples were measured with the PerkinElmer Spectrometer (PerkinElmer, UK) with the accessory of attenuated total reflectance (ATR) in a range of 4000 and 600 cm^{-1}, utilizing 16 scans per measurement. To correct spectra with sloped baselines and reduce the amount of noise in the spectrum, a baseline correction and smoothing process was conducted after sample measurements using the software (TA Instruments).

Unidirectional and Thickness Swelling Ratio Calculation: Pollen paper was cut into several small pieces of size 1.5 × 2 mm and then treated with different pH levels (2, 4, 6, 8, 10, and 12) for 2 h. Microscope photos of the small pollen papers were taken after different treatment conditions. Image J (National Institute of Health, Bethesda, MD, USA) was used to measure the lengths of their long sides. The thicknesses at different states were measured with a digital micrometer. The percentage of their unidirectional and thickness swelling ratio in the hydrated (R_{wet} and T_{wet}) state and redry (R_{dry} and T_{dry}) state was calculated using the following equations:

$$R_{wet}\,(\%) = (L_1 - L_0)\,/L_0 \times 100 \quad (1)$$

$$R_{dry}\,(\%) = (L_2 - L_0)\,/L_0 \times 100 \quad (2)$$

$$T_{wet}\,(\%) = (T_1 - T_0)\,/T_0 \times 100 \quad (3)$$

$$T_{dry}\,(\%) = (T_2 - T_0)\,/L_0 \times 100 \quad (4)$$

where R is the unidirectional swelling ratio, and T is the thickness swelling ratio; L_0 and T_0 are the length and thickness of dry small pollen papers after pH treatment. Then, the dry samples were immersed in DI water for 1 h to obtain the hydrated state. L_1 and T_1 are the length and thickness of the samples in the hydrated state. The hydrated small pollen papers were redried under an ambient environment, and their length (L_2) and thickness (T_2) were measured in a redry state.

Tensile Testing: The tensile mechanical tests under an ambient environment (RH 60%, 28 °C) were conducted using a dynamic mechanical analyzer (DMA Q800, TA Instruments). The thin pollen paper samples (25 mm × 5 mm × 0.07 mm) were gripped in a film tension clamp, and the tensile tests were carried out under the ramp force 1 N min^{-1} until failure. To control RH during mechanical tensile tests, we used a DMA Q800 equipped with the DMA-RH Accessory to perform the tensile tests under a specific RH of 20%. Each test was repeated three times to get the average value. The Young's modulus of the pollen sample was calculated from the slope of the elastic ranges in the stress - strain curves. All data were analyzed using Universal Analysis 2000 software (TA Instruments).

The Hygroscopicity-Induced Unidirectional Strain of Pollen Paper: DMA Q800 equipped with the DMA-RH Accessory was used to measure the unidirectional strain of different pH-treated pollen papers as RH decreased from 70% to set values (20%, 30%, 40%, and 50%). The following measurement method was conducted: 1) stress = 0.01 MPa (make sure the pollen paper is straight); 2) RH x % (x = 20%, 30%, 40%, or 50%); 3) Isothermal for 20.00 min (allow the system reach the RH setup); 4) Measure Length; 5) Data storage On; 6) Isothermal for 20.00 min (allows time for the sample to equilibrate under set RH level). Each test was repeated three times to get the average value.

Coiling Behavior of the Patterned Bilayer Pollen Actuators in Response to Changing RH: Patterned pollen bilayer actuators (6.2 cm × 0.5 cm) were hung in a chamber. The specific RH level in the chamber was made by a saturated salt aqueous solution, CH_3COOK (RH = 23%). The RH level in the ambient environment is ≈60%. The coiling behavior was recorded by an iPhone 15 Pro Max (1920 × 1080-pixel resolution, 60 frames per second, Apple Inc.)

One Pot Reprogramming Process of Bilayer Pollen Actuators: The patterned bilayer pollen paper was first immersed in a basic buffer solution (pH 12) for 5 min to swell and remove the toner fragments on the surface. Then, the clean pollen paper was transferred into DI water to wash for 5 min. Finally, the hydrated pollen paper was left to dry in ambient air overnight for reprogramming.

Curvature Calculation: The different pH-treated bilayer pollen actuators (0.5 cm × 2.5 cm) with toner pattern orientation ($\theta = 90°$) were hung in a chamber. The specific RH level in the chamber was made by a saturated salt aqueous solution, CH_3COOK (RH = 23%). After the papers reached the steady-state bending, they were placed back in another chamber with a saturated salt solution, NaCl (RH = 70%), until all of them returned to their original shape. The entire process was recorded by the iPhone 14 Pro Max. Curvature, κ, was calculated as below:

$$\kappa = \pi\alpha/180°L \quad (5)$$

where α is the bending angle, directly measured from the captured images of recorded videos, and L is the paper-free bending length.

Supporting Information

Supporting Information is available from the Wiley Online Library or from the author.

Acknowledgements

The authors thank Mr Ervin Wong Tim for contributions to partial data collection. This work was supported by the Ministry of Education (MOE) grant MOE-MOET32022-0002, Global Green Growth Institute (GGGI)-REQ0412626. The research was also supported by the Korea Institute of Planning and Evaluation for Technology in Food, Agriculture, and Forestry(IPET) -through a research collaboration agreement between RE:harvestCo., Ltd. and Nayang Technological University (REQ0639147). This work was also supported by the National Natural Science Foundation of China (no. 52303131).

Conflict of Interest

The authors declare no conflict of interest.

Data Availability Statement

The data that support the findings of this study are available from the corresponding author upon reasonable request.

Keywords

3D geometrical encryption carriers, bilayer actuator, dual regulation, natural pollen materials, re-programmability

Received: August 3, 2025
Revised: October 24, 2025
Published online:

[1] R. Yang, M. Jin, M. Jin, H. Qian, Q. Gao, G. Jin, S. Zhang, *Adv. Intell. Syst.* **2020**, *3*, 2000146.
[2] C. Ni, D. Chen, X. Wen, B. Jin, Y. He, T. Xie, Q. Zhao, *Nat. Commun.* **2023**, *14*, 7672.
[3] X. Chen, D. Goodnight, Z. Gao, A. H. Cavusoglu, N. Sabharwal, M. DeLay, A. Driks, O. Sahin, *Nat. Commun.* **2015**, *6*, 7346.
[4] L. Ren, B. Li, K. Wang, X. Zhou, Z. Song, L. Ren, Q. Liu, *Front. Mater.* **2021**, *8*, 651521.
[5] Q. L. Zhu, C. Du, Y. Dai, M. Daab, M. Matejdes, J. Breu, W. Hong, Q. Zheng, Z. L. Wu, *Nat. Commun.* **2020**, *11*, 5166.
[6] S. Wu, Y. Hong, Y. Zhao, J. Yin, Y. Zhu, *Sci. Adv.* **2023**, *9*, adf8014.
[7] X. Qiu, Q. Guo, Y. Wang, X. Huang, J. Cao, Z. Zheng, X. Zhang, *ACS Appl. Mater. Interfaces* **2020**, *12*, 41981.
[8] X. Pan, N. Grossiord, J. A. H. P. Sol, M. G. Debije, A. P. H. J. Schenning, *Adv. Funct. Mater.* **2021**, *31*, 2100465.
[9] Y. Zhang, X. Zhou, L. Liu, S. Wang, Y. Zhang, M. Wu, Z. Lu, Z. Ming, J. Tao, J. Xiong, *Adv. Mater.* **2024**, *36*, 2404696.
[10] K. Guo, M. Liu, D. Vella, S. Suresh, K. J. Hsia, *Proc. Natl. Acad. Sci. USA* **2024**, *121*, 2320259121.
[11] B. Han, Z. C. Ma, Y. L. Zhang, L. Zhu, H. Fan, B. Bai, Q. D. Chen, G. Z. Yang, H. B. Sun, *Adv. Funct. Mater.* **2021**, *32*, 2110997.
[12] Y. Wang, Z. Wang, Q. He, P. Iyer, S. Cai, *Adv. Intell. Syst.* **2020**, *2*, 1900177.
[13] Z. Chen, B. Gao, P. Li, X. Zhao, Q. Yan, Z. Liu, L. Xu, H. Zheng, F. Xue, R. Ding, J. Xiong, Z. Tang, Q. Peng, Y. Hu, X. He, *ACS Nano* **2023**, *17*, 23032.
[14] A. M. Abdullah, X. Li, P. V. Braun, J. A. Rogers, K. J. Hsia, *Adv. Mater.* **2018**, *30*, 1801669.
[15] S. Xiao, M. Zhang, X. He, L. Huang, Y. Zhang, B. Ren, M. Zhong, Y. Chang, J. Yang, J. Zheng, *ACS Appl. Mater. Interfaces* **2018**, *10*, 21642.
[16] T. Zhao, W. Dou, Z. Hu, W. Hou, Y. Sun, J. A. Lv, *Macromol. Rapid Commun.* **2020**, *41*, 2000313.
[17] S. Wang, Y. Gao, A. Wei, P. Xiao, Y. Liang, W. Lu, C. Chen, C. Zhang, G. Yang, H. Yao, T. Chen, *Nat. Commun.* **2020**, *11*, 4359.
[18] D. D. Han, Y. L. Zhang, J. N. Ma, Y. Q. Liu, B. Han, H. B. Sun, *Adv. Mater.* **2016**, *28*, 8328.
[19] M. D. Pozo, J. Sol, S. H. P. van Uden, A. R. Peeketi, S. J. D. Lugger, R. K. Annabattula, A. Schenning, M. G. Debije, *ACS Appl. Mater. Interfaces* **2021**, *13*, 59381.
[20] Y. Zhang, C. Zhang, R. Wang, W. Tan, Y. Gu, X. Yu, L. Zhu, L. Liu, *Soft Matter* **2022**, *18*, 5725.
[21] M. Lalegani Dezaki, M. Bodaghi, *Int J. Prec. Eng. Man.-Green Technol.* **2023**, *10*, 1661.
[22] Y. Zheng, H. Huang, Y. Wang, J. Zhu, J. Yu, Z. Hu, *Sens. Actuators, B* **2021**, *349*, 130735.
[23] L. Sun, Q. Zhao, L. Che, M. Li, X. Leng, Y. Long, Y. Lu, *Adv. Funct. Mater.* **2023**, *34*, 2311398.
[24] J. Xiao, H. Liu, S. Wang, S. Ma, L. Zhang, Y. Qi, *Adv. Funct. Mater.* **2024**, *34*, 2316301.
[25] S. J. A. Houben, S. J. D. Lugger, R. J. H. van Raak, A. P. H. J. Schenning, *ACS Appl. Polym. Mater.* **2022**, *4*, 1298.
[26] A. H. Gelebart, D. J. Mulder, G. Vantomme, A. Schenning, D. J. Broer, *Angew. Chem. Int. Ed. Engl.* **2017**, *56*, 13436.
[27] G. Gao, K. Yin, J. Han, Y. Hu, J. Gu, J. Wei, T. Chen, *Angew. Chem. Int. Ed. Engl.* **2024**, *64*, 202416672.
[28] Z. Zhao, J. Deng, H. Tae, M. S. Ibrahim, S. Suresh, N. J. Cho, *Adv. Mater.* **2022**, *34*, 2109367.
[29] Z. Zhao, Y. Hwang, Y. Yang, T. Fan, J. Song, S. Suresh, N. J. Cho, *Proc. Natl. Acad. Sci. USA* **2020**, *117*, 8711.
[30] J. Deng, Z. Zhao, X. Y. Yeo, C. Yang, J. Yang, A. R. Ferhan, B. Jin, C. Oh, S. Jung, S. Suresh, N. J. Cho, *Adv. Mater.* **2024**, *36*, 2311684.
[31] Z. Zhao, J. Kumar, Y. Hwang, J. Deng, M. S. B. Ibrahim, C. Huang, S. Suresh, N. J. Cho, *Proc. Natl. Acad. Sci. USA* **2021**, *118*, 2113715118.
[32] F. Liu, Y. Wu, M. Zheng, Y. Liu, S. Cao, Y. Qiu, Z. Zhao, H. Deng, *Adv. Funct. Mater.* **2025**, *35*, 2418911.
[33] Y. Qiu, D. Zhang, M. Long, Z. Zhou, C. Gao, S. Ma, J. Qin, K. Chen, C. Chen, Z. Zhao, *Sci. Adv.* **2025**, *11*, adr1596.
[34] C. Huang, Z. Wang, D. Quinn, S. Suresh, K. J. Hsia, *Proc. Natl. Acad. Sci. USA* **2018**, *115*, 12359.
[35] T. F. Fan, S. Park, Q. Shi, X. Zhang, Q. Liu, Y. Song, H. Chin, M. S. B. Ibrahim, N. Mokrzecka, Y. Yang, H. Li, J. Song, S. Suresh, N. J. Cho, *Nat. Commun.* **2020**, *11*, 1449.
[36] F. Liu, Y. Wu, M. Zheng, Y. Liu, S. Cao, Y. Qiu, Z. Zhao, H. Deng, *Adv. Funct. Mater.* **2025**, *35*, 2418911.
[37] K. Saito, T. Xu, H. Ishikita, *J. Phys. Chem. B* **2022**, *126*, 4999.
[38] A. R. Attar, D. E. Blumling, K. L. Knappenberger, Jr., *J. Chem. Phys.* **2011**, *134*, 024514.
[39] J. Li, E. Ma, *Cellulose* **2024**, *31*, 8445.
[40] S. Khoshtinat, V. Carvelli, C. Marano, *Cellulose* **2023**, *30*, 7779.
[41] S. Taccola, F. Greco, E. Sinibaldi, A. Mondini, B. Mazzolai, V. Mattoli, *Adv. Mater.* **2015**, *27*, 1668.